

Image based aberration retrieval using helical point spread functions

Berlich, René; Stallinga, Sjoerd

DOI

[10.1364/AO.396140](https://doi.org/10.1364/AO.396140)

Publication date

2020

Document Version

Final published version

Published in

Applied Optics

Citation (APA)

Berlich, R., & Stallinga, S. (2020). Image based aberration retrieval using helical point spread functions. *Applied Optics*, 59(22), 6557-6572. <https://doi.org/10.1364/AO.396140>

Important note

To cite this publication, please use the final published version (if applicable). Please check the document version above.

Copyright

Other than for strictly personal use, it is not permitted to download, forward or distribute the text or part of it, without the consent of the author(s) and/or copyright holder(s), unless the work is under an open content license such as Creative Commons.

Takedown policy

Please contact us and provide details if you believe this document breaches copyrights. We will remove access to the work immediately and investigate your claim.

Green Open Access added to TU Delft Institutional Repository

'You share, we take care!' - Taverne project

<https://www.openaccess.nl/en/you-share-we-take-care>

Otherwise as indicated in the copyright section: the publisher is the copyright holder of this work and the author uses the Dutch legislation to make this work public.



Image based aberration retrieval using helical point spread functions

RENÉ BERLICH^{1,*}  AND SJOERD STALLINGA² 

¹Fraunhofer Institute for Applied Optics and Precision Engineering, Albert-Einstein Str. 7, 07745 Jena, Germany

²Department of Imaging Physics, Delft University of Technology, Lorentzweg 1, 2628 CJ Delft, The Netherlands

*Corresponding author: rene.berlich@iof.fraunhofer.de

Received 24 April 2020; revised 8 June 2020; accepted 30 June 2020; posted 30 June 2020 (Doc. ID 396140); published 27 July 2020

A practical method for determining wavefront aberrations in optical systems based on the acquisition of an extended, unknown object is presented. The approach utilizes a conventional phase diversity approach in combination with a pupil-engineered, helical point spread function (PSF) to discriminate the aberrated PSF from the object features. The analysis of the image's power cepstrum enables an efficient retrieval of the aberration coefficients by solving a simple linear system of equations. An extensive Monte Carlo simulation is performed to demonstrate that the approach makes it possible to measure low-order Zernike modes including defocus, primary astigmatism, coma, and trefoil. The presented approach is tested experimentally by retrieving the two-dimensional aberration distribution of a test setup by imaging an extended, unknown scene. © 2020 Optical Society of America

<https://doi.org/10.1364/AO.396140>

1. INTRODUCTION

Optical aberrations limit the performance of imaging and illumination systems in terms of resolution and signal-to-noise ratio (SNR). Even well-optimized and toleranced optical designs may still be subject to severe aberrations when put into practice. Depending on the particular application scenario, this is due to external effects such as mechanically or thermally induced deformations, atmospheric turbulence or residual misalignment (i.e., for segmented mirrors), and manufacturing tolerances. These effects can be mitigated by means of adaptive optics or dedicated image post processing, which generally require detailed knowledge of the aberrations and ultimately the wavefront. The most common concepts for measuring the wavefront utilize interferometers or Shack–Hartman sensors. An alternative approach with a lower hardware complexity relies on the direct analysis of the effect of the aberrations on the point spread function (PSF) of the system. Existing methods are based mainly on iterative Fourier transform or maximum-likelihood estimation (MLE) methods that determine the wavefront phase from a single PSF image or a through-focus PSF stack [1–4]. The estimation can be performed with high numerical efficiency in the approximation of small aberrations and low-NA optical systems using a linear system approach [5–8]. Machine learning offers alternative approaches that have gained increased interest in recent years. Using proper training sets and artificial neural networks, it has been shown that aberrations can be retrieved from image intensity measurements [9–13]. Yet, most of the proposed intensity based methods are applicable only to point sources [3–12], and only a few consider simplified objects such

as a sphere or single letters [13]. Moreover, they provide the aberration information for only a single dedicated field point.

Such distinct objects, however, are not always available in applications such as surveillance, microscopy, or Earth observation. Also, the respective optical systems feature an extended field of view with field dependent aberrations. In order to estimate the (field dependent) aberrations for an unknown scene, the object features need to be separated from the PSF, which provides the information on the aberration. One widely studied method to accomplish this is phase diversity (PD) [14,15], which is based on a MLE [14–17], image contrast optimization [18], or other metrics [19,20]. It has been applied for the co-phasing of segmented mirrors [19,21] or high-resolution coronagraphic imaging [22]. In general, the PD methods that consider an extended object scene necessitate numerically expensive, iterative optimization procedures that prohibit real-time (snapshot) measurements. Moreover, they require *a priori* assumptions on the object spectrum, as well as a careful choice of optimization parameters and regularization measures [17], which significantly influence their performance. A modified PD method is based on the analysis of the change in image intensity distribution introduced by an adaptive optical component [23,24]. The approach requires little *a priori* knowledge of the object but necessitates specialized adaptive-optical hardware and multiple, iterative image acquisition steps. A linear aberration retrieval model that eliminates the need for an iterative optimization in the case of an extended object has been proposed by Mocoer *et al.* [25]. However, the applicability of this method in practice is not demonstrated, since the

authors neither provide a general numerical demonstration of the method for multiple sets of objects and aberrations, nor perform an experimental proof of concept. A recently proposed, non-iterative aberration retrieval method for extended scenes utilizes a combination of PD and deep learning [26]. Yet, the approach can be applied only if image noise is negligible, as otherwise the incorporated image processing routine becomes numerically unstable. Additionally, the approach has been demonstrated experimentally for simplified extended objects, i.e., single numbers, only.

In this paper, we introduce a novel approach that extends the conventional PD concept using helical PSFs, which are used for three-dimensional localization and imaging [27–29]. These PSFs typically consist of a number of well-identifiable sub-peaks that rotate around the focal point as a function of defocus. In Ref. [30], it is shown that aberrations distort the PSF sub-peak positions and ultimately influence their rotation angle. Therefore, they deteriorate the depth measurement accuracy of such pupil engineered (PE) systems. In contrast to previous work, this dependency is actually exploited in the approach presented here in order to retrieve information on the aberrations that are present.

At first, the general concept of PEPD using helical PSFs is introduced. A linear model is derived, which enables the direct retrieval of aberrations without the need for iterative optimization or blind deconvolution. Then, a numerical assessment is conducted for an exemplary PEPD system, which quantifies the performance of the proposed method considering low-order aberrations for unknown, natural objects. In particular, we analyze theoretical precision limits provided by the Cramér–Rao lower bound (CRLB) as well as the aberration retrieval success rate (SR), which represents a suitable figure of merit for practical imaging applications. Finally, an experimental proof of concept is demonstrated by measuring low-order aberration coefficients for a misaligned optical system considering a point source as well as an extended object.

2. PUPIL ENGINEERED PHASE DIVERSITY

The general PD concept for measuring an aberrated wavefront is based on capturing a number of M images of the same object distribution $o(\mathbf{x})$. Each of these images $i_m(\mathbf{x})$ is obtained by introducing a known phase distribution $\phi_{d,m}(\mathbf{u})$, referred to as PD. Here, \mathbf{x} and \mathbf{u} denote the image plane and pupil plane coordinates, respectively. The imaging process for each configuration m , referred to as channels, can be described by the following convolution:

$$i_m(\mathbf{x}) = \underbrace{K_m o_{\text{norm}}(\mathbf{x}) * h_m(\mathbf{x})}_{\tilde{i}_m(\mathbf{x})} + v_m(\mathbf{x}), \quad (1)$$

where $o_{\text{norm}}(\mathbf{x})$ is the normalized object distribution, and $\tilde{i}_m(\mathbf{x})$ is the signal of the m th channel in the absence of noise. The number of photons per channel is denoted by K_m , the image noise is described by $v_m(\mathbf{x})$, and $h_m(\mathbf{x})$ is the PSF. The latter is obtained by taking the absolute square of the Fourier transformation of the pupil function $g_m(\mathbf{u})$ according to

$$\begin{aligned} h_m(\mathbf{x}) &= |\mathcal{F}[g_m(\mathbf{u})]|^2 \\ &= |\mathcal{F}[A(\mathbf{u}) \exp[i(\phi_m(\mathbf{u}))]]|^2, \end{aligned} \quad (2)$$

i.e., we assume incoherent imaging conditions. The amplitude function $A(\mathbf{u})$ corresponds to a circular transmission window and is assumed to be equal for all channels. The pupil phase $\phi_m(\mathbf{u})$ of each channel is a result of the superposition of the wavefront aberration ϕ_a and the introduced diversity $\phi_{d,m}$. In accordance with the conventional PD approach, both contributions are decomposed into Zernike modes Z_n according to

$$\begin{aligned} \phi_m(\mathbf{u}) &= \phi_a(\mathbf{u}) + \phi_{d,m}(\mathbf{u}) \\ &= \sum_n (\alpha_n + \Delta_{n,m}) Z_n(\mathbf{u}), \end{aligned} \quad (3)$$

where n labels the different contributing Zernike modes. The aberration retrieval using the conventional PD method then corresponds to retrieving the coefficients α_n , which are equal for all channels m , by introducing known diversity coefficients $\Delta_{n,m}$. The first three Zernike modes (piston, tip, and tilt) are excluded, as they cannot be accessed directly using PD, which is a common limitation of the technique. In order to retrieve higher-order coefficients, multiple estimation approaches based on MLE [14,16], image contrast optimization [18], or alternative metrics [19,20] have been introduced and applied. All of these require iterative optimization procedures that prohibit fast, real-time measurements (e.g., in a closed-loop) for high-resolution images with a sampling on the order of megapixels.

We propose the use of pupil engineering to overcome these restrictions of conventional PD. To this end, an additional phase term $\phi_{\text{PE}}(\mathbf{u})$ is added to Eq. (3), and the pupil phase $\phi_m(\mathbf{u})$ of the m th channel is then given by

$$\phi_m(\mathbf{u}) = \sum_n (\alpha_n + \Delta_{n,m}) Z_{n,m}(\mathbf{u}) + \phi_{\text{PE}}(\mathbf{u}). \quad (4)$$

The PE term $\phi_{\text{PE}}(\mathbf{u})$ is assumed to be equal for all channels. It can thus be realized using a single phase element, which simplifies the practical implementation and eliminates systematic errors due to different tolerances of the elements. The most common diversity implementation, which is also assumed for the PEPD method proposed here, incorporates a known defocus aberration Δ_4 between $M=2$ different imaging configurations. The choice of this configuration is motivated primarily by practical considerations, as this can be realized relatively easily by a sequential shift of the image distance or by using a beam splitting configuration, which allows for capturing the two images at the same time. The PEPD configuration is shown schematically in the top part of Fig. 1.

Here, the goal of the additional phase term ϕ_{PE} in Eq. (4) is to eliminate the need for iterative retrieval methods by generating a PSF that makes a decoupling of object and aberration (PSF) information possible. This can be achieved using phase elements [i.e., computer generated holograms (CGHs)], which lead to helical PSFs that rotate through defocus, because of two unique characteristics of such a PSF. First, helical PSFs provide a distinct shape distortion in the presence of low-order aberrations

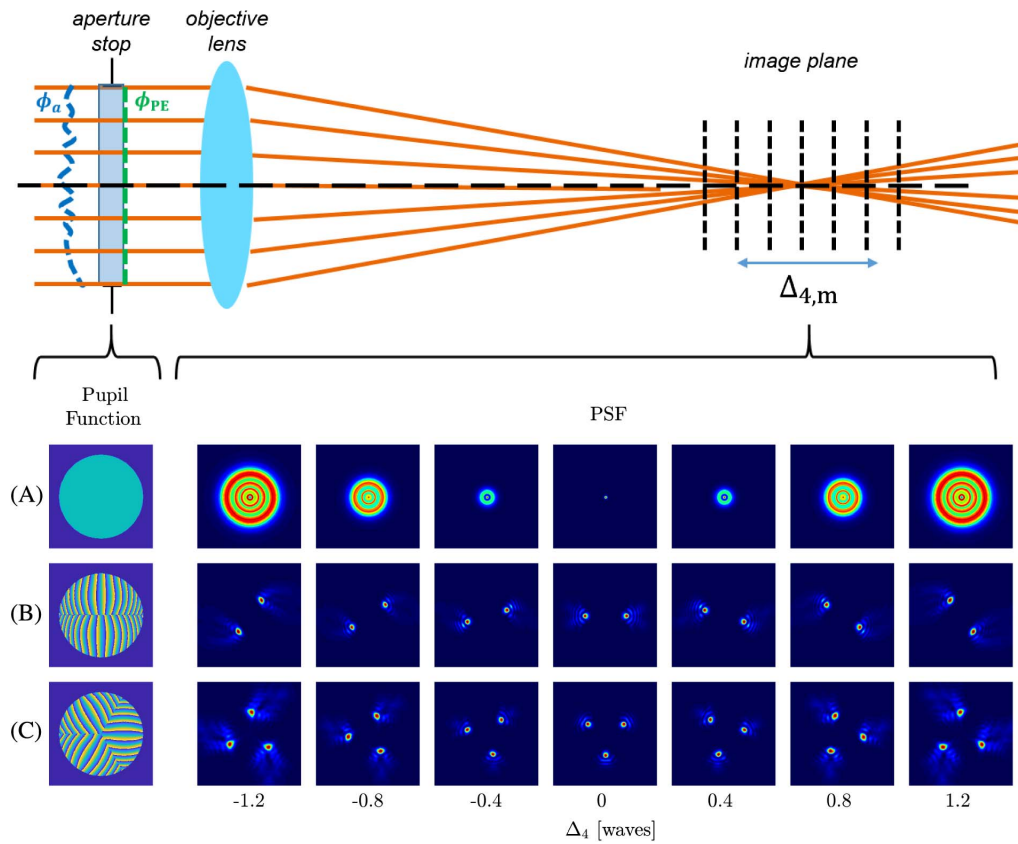


Fig. 1. Top: schematic setup overview of the proposed PEPD approach for aberration retrieval. Bottom: PSF dependency on the defocus diversities Δ_4 for different pupil functions that generate (a) nominal PSF, and (b) double- and (c) triple-helix PSFs.

that can be retrieved even in the case of an extended object. In conventional PD, the required image diversity is introduced by an aberration dependent blurring of the PSF, which depends on the defocus coefficient $\Delta_{4,m}$. In general, the complex relationship between this blur and the aberrated pupil phase $\phi_m(\mathbf{u})$ necessitates the use of iterative blind deconvolution methods for an extended, unknown object distribution. In contrast, helical PSFs exhibit distinct shifts of the PSF peaks as described in Ref. [30] depending on the particular aberration coefficient α_n and the defocus diversity $\Delta_{4,m}$. These shifts are encoded in the acquired images $i_m(\mathbf{x})$ of the extended object and can be retrieved using the cepstrum approach presented in Ref. [31]. The second unique characteristic of helical PSFs is illustrated in the bottom part of Fig. 1 for two particular examples of double- and triple-helix PSFs. The PSFs provide an inherent peak rotation for different amounts of defocus diversities $\Delta_{4,m}$ while preserving the confined shape of the individual peaks. This feature can be utilized to diversify the PSF response to individual aberration coefficients α_n and to eliminate ambiguities by acquiring two images with different diversities $\Delta_{4,m}$. All things considered, these two properties enable a unique retrieval of aberration coefficients α_n by measuring peak shifts for two defocus diversities. The idea of using helical PSFs for aberration retrieval based on a through-focus measurement has been previously applied in Ref. [32]. The practicality of that approach is limited since it requires the acquisition of three subsequent image stacks ($M > 30$) and it is applicable only to point objects.

3. LINEAR ABERRATION RETRIEVAL MODEL

The aberration retrieval is based on exploiting the effect of different aberrations on the PSF shape. Aberrations generally lead to a spreading of a conventional PSF. It turns out, however, that low-order aberrations lead to a shift of the individual peaks in the case of a helical PSF [30]. In particular, defocus, astigmatism, and spherical aberration lead to an overall rotation of a double-helix PSF. In contrast to previous work, which analyzed only the aberration effect on the overall PSF rotation angle, the individual location $(x_j^{\text{PSF}}, y_j^{\text{PSF}})$ of each PSF peak is now considered.

In the PEPD approach described in the previous section, the PSF $h_m(x)$ is not directly accessible from the measured image irradiance $i_m(x)$ when an unknown, extended object is considered. However, the approach described in Ref. [31] can be utilized to obtain the helical PSF peak locations $(x_j^{\text{PSF}}, y_j^{\text{PSF}})$. It is based on retrieving the location (x_j^c, y_j^c) of peaks in the power cepstrum distribution of the acquired, PE image. These peaks can be associated with the helical PSF peak positions, if the object contains small spatial features with a size that is comparable to or smaller than the helical PSF (projected in object space) as elaborated in Ref. [31]. Under this condition, the aberration retrieval method proposed here is based on analyzing the change of the power cepstrum's peak positions due to aberrations. In general, a larger number J of PSF peaks results in a larger number of degrees of freedom. Yet, the larger the peak number J , the more complex the cepstrum analysis, which

contains $J(J - 1)/2$ peaks to be identified. Further, a larger value for J results in a smaller maximum range of aberration coefficients that can be retrieved without ambiguities. Only triple-helix PSFs are therefore considered here, which provide a practical compromise between the maximization of the number of degrees of freedom and robust cepstrum peak identification.

In the following, the influence of the first eight Zernike aberrations (excluding piston, tip, and tilt) on the cepstrum peak positions (x_j^c, y_j^c) with $j = [1, 2, 3]$ is assessed. These aberrations are defocus (Z_4), primary astigmatism (Z_5, Z_6), coma (Z_7, Z_8), trefoil (Z_9, Z_{10}), and spherical aberration (Z_{11}). The cepstrum distribution of the aberrated PSF is calculated for each individual aberration coefficient in a range of

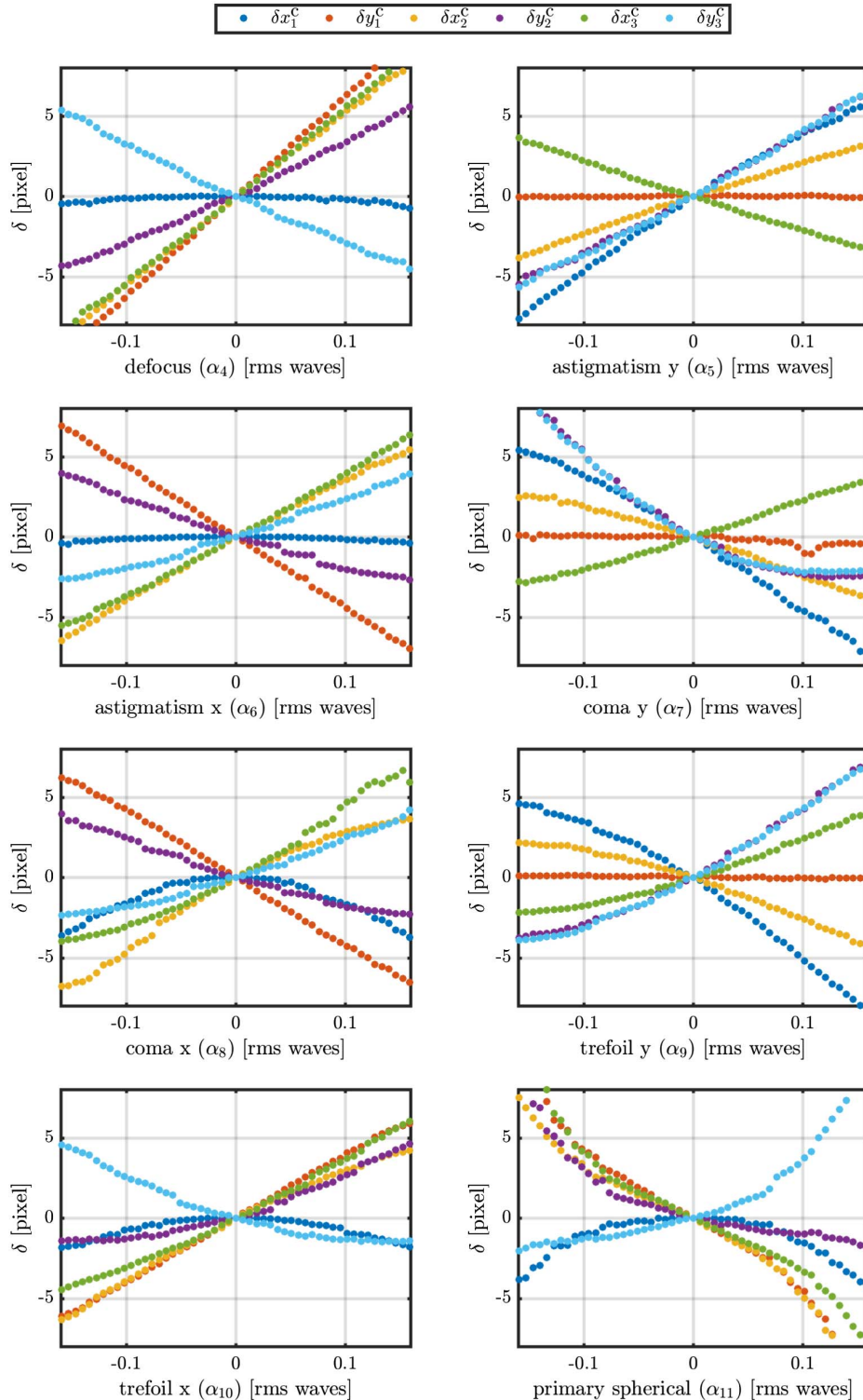


Fig. 2. Dependency of cepstrum peak location shift ($\delta x_j^c, \delta y_j^c$) on the coefficients α_n of low-order Zernike aberrations ($N \leq 8$), excluding piston, tip, and tilt.

$\alpha_n = [-0.16, 0.16]$ waves rms. The peak positions are extracted by processing the cepstrum distribution and performing a Gaussian peak fit as described in Ref. [31]. The dependencies of the position changes ($\delta x_j^c, \delta y_j^c$) are exemplarily plotted in Fig. 2 for an in-focus diversity channel ($\Delta_4 = 0$ waves). The same set of parameters describing the optical system will be used throughout the theoretical and numerical investigations in this paper.

It can be seen that the aberration coefficients α_n lead to a close to linear change of the PSF parameters for the coefficient range of approximately $\alpha_n = [-0.1, 0.1]$. Hence, the PEPD approach is described by a linear system model, and the effect of an aberration vector α on the PSF peak locations $(\mathbf{x}^c, \mathbf{y}^c)_m$ of a particular channel m is approximated by a linear transfer matrix \hat{T}_m according to

$$\begin{aligned} \begin{pmatrix} \mathbf{x}^c(\alpha) \\ \mathbf{y}^c(\alpha) \end{pmatrix}_m &= \begin{pmatrix} \mathbf{x}^c \\ \mathbf{y}^c \end{pmatrix}_{m,0} + \begin{pmatrix} \delta \mathbf{x}^c(\alpha) \\ \delta \mathbf{y}^c(\alpha) \end{pmatrix}_m \\ &= \begin{pmatrix} \mathbf{x}^c \\ \mathbf{y}^c \end{pmatrix}_{m,0} + \hat{T}_m \cdot \alpha, \end{aligned} \quad (5)$$

where $(\mathbf{x}^c, \mathbf{y}^c)_{m,0}$ denotes the nominal cepstrum peak location when no aberrations are present. Note that the size of the transfer matrix \hat{T}_m is $6 \times N$, where N is the number of Zernike modes to be retrieved. The determination of the linear model parameters, which include the nominal cepstrum vector $(\mathbf{x}^c, \mathbf{y}^c)_{m,0}$ as well as the elements of the transfer matrix \hat{T}_m , can be understood as a necessary calibration procedure for the

PEPD system. These parameters could be obtained experimentally by introducing a set of known aberrations to the system. Although this approach provides a high robustness with respect to intrinsic tolerances of a real system, such a pre-defined set is not always accessible. An alternative approach is based on using a theoretical model of the optical system design and performing purely numerical simulations of the aberration influence as performed in Fig. 2. To this end, the nominal peak vectors as well as the transfer matrix can be obtained by fitting linear functions to the simulated dependencies $(x_j^c(\alpha), y_j^c(\alpha)_m)$ for each peak i and channel m . We consider a particular aberration coefficient fit range of approximately $\alpha_n = [-0.1, 0.1]$ waves rms, where a close to linear dependency is maintained for all Zernike modes under consideration. As can be seen in Fig. 2, the deviation from this linear approximation is significantly increased for larger coefficients, i.e., for spherical aberration, coma, and trefoil, which results in a reduced accuracy of the linear aberration retrieval model.

An aberration vector α can now be estimated based on only two calculation steps using the linear model described by Eq. (5). First, the PSF peak locations $(\mathbf{x}^c(\alpha), \mathbf{y}^c(\alpha))_m$ are calculated for the measured images $i_m(\mathbf{x})$ using the cepstrum approach described in Ref. [31]. Second, the linear system in Eq. (5) is solved by taking the pseudo-inverse of the transfer matrix \hat{T} . This direct approach enables fast aberration retrieval even for high-resolution images. The obtained solution may be subject to a large estimation error though, if the linear system is not well conditioned. The condition number provides a measure to compare the relative estimation errors for different

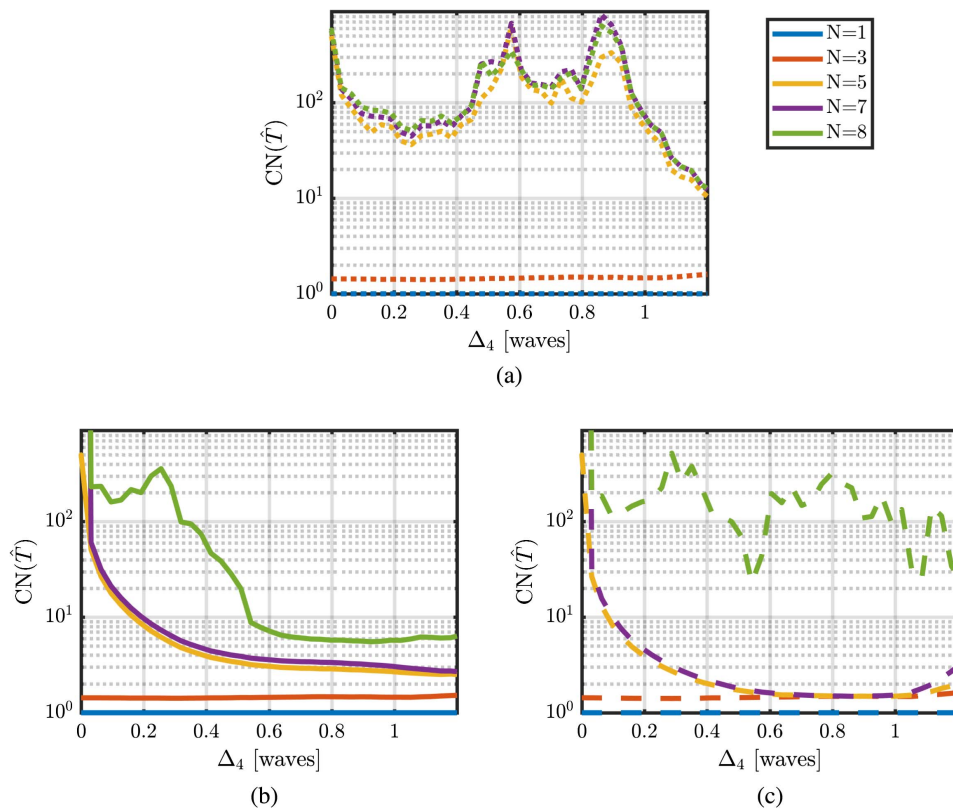


Fig. 3. Dependency of the condition number $CN(\hat{T})$ on the defocus diversity Δ_4 for retrieving up to N Zernike modes and considering different PD configurations. (a) Single channel, (b) two asymmetric channels, and (c) two symmetric channels.

PEPD scenarios and to assess under what condition an aberration vector α cannot be retrieved reliably. Figure 3(a) shows the dependency of the condition number $\text{CN}(\hat{T}_m)$ on the defocus diversity Δ_4 for a single-channel PEPD aberration retrieval of up to N Zernike modes. Note that only positive values of Δ_4 are plotted in view of the symmetry of $\text{CN}(\hat{T}_m)$. The dependency is analyzed only for defocus diversities up to $\Delta_4 = 1.2$ waves. Larger defocus values lead to significant spreading of the triple-helix PSF, which prevents a reliable cepstrum peak identification. The graphs in Fig. 3(a) show that a low condition number is provided only for the retrieval of up to three modes throughout the entire defocus diversity range of interest. In other words, only defocus and astigmatism can be reliably retrieved using the proposed PEPD approach based on a single measurement. In fact, the depth retrieval approach described in Ref. [31] represents the particular case of retrieving the defocus aberration only, where other aberrations are considered negligible.

In order to retrieve more than three Zernike orders, at least two channels need to be considered because with a single channel, there are not enough degrees of freedom in the linear PSF peak shift model and the solution becomes ambiguous. This is analogous to the conventional PD approach. To this end, the linear model in Eq. (5) is extended by simply combining the rows of the measured peak positions $(\mathbf{x}^c(\alpha), \mathbf{y}^c(\alpha))_m$, the nominal peak positions $(\mathbf{x}^c, \mathbf{y}^c)_{m,0}$, and the transfer matrix \hat{T}_m . Figure 3 shows the dependency of the condition number of the extended transfer matrix for two commonly investigated, two-channel PD configurations ($M=2$). The asymmetric configuration [Fig. 3(b)] utilizes one channel in focus and one channel that is defocused by the amount Δ_4 . Conversely, the symmetrical approach [Fig. 3(c)] is based on two image planes around the nominal focus location, which are subject to a defocus diversity of $\pm\Delta_4$, respectively. Both configurations result in significantly reduced condition numbers for $N=[5, 7]$ compared to the single-channel configuration. The symmetrical configuration provides the lowest, overall condition number of $\text{CN}(\hat{T}) = 1.4$ at $\Delta_4 = 0.8$ waves for the retrieval of up to $N=7$ modes and the defocus range of interest. A reduced condition number for $N=8$ modes, which includes spherical aberration, can be obtained only using the asymmetrical configuration and defocus diversities $\Delta_4 > 0.5$ waves. Yet, the corresponding minimum achievable condition number of $\text{CN}(\hat{T}) = 5.5$ already indicates that the retrieval using the proposed PEPD approach is subject to considerable estimation errors in that case.

4. NUMERICAL PERFORMANCE ASSESSMENT

A. Monte Carlo Analysis

The following numerical investigations are based on the optical layout shown in Fig. 1. The optical design parameters are selected based on the experimental demonstration system that is used in Section 5. The optical system is characterized by an aperture stop diameter of 10 mm, which is located in front of a focusing lens with a focal length of 150 mm. A wavelength of 540 nm is considered, and the object is assumed to be located 1.8 m in front of the aperture stop, which results in an image space F-number of 15.9. The applied pixel size of

3.45 μm ensures a proper sampling with a Nyquist sampling frequency of 145 lp/mm above the optical cutoff frequency of $\rho_{\text{cut-off}} = 117$ lp/mm. The triple-helix PSF phase element shown in Fig. 1 is used as a baseline for the PEPD approach evaluation. In addition, a double-helix PSF is considered for comparison purposes. The particular designs of both phase elements are equal to the designs used in Ref. [30]. Figure 1 shows the dependency of the conventional as well as the PE PSFs on the defocus diversity Δ_4 . Note that a geometrical image shift of 1 mm corresponds approximately to an rms defocus value of $\Delta_4 = 0.27$ waves.

In addition to the image noise $v_m(\mathbf{x})$, the precision of the PD aberration retrieval depends strongly on the specific PD settings including the amount of defocus diversity Δ_4 , the particular aberrations to be estimated α , as well as the observed object distribution $o(\mathbf{x})$. Accordingly, a numerical Monte Carlo type analysis is performed in order to compare different PD settings and to assess general performance limits of the proposed PEPD method. So far, numerical studies in this area assumed either solely additive Gaussian noise [33–35] (i.e., camera readout noise) or pure Poisson noise [34] (photon shot-noise). Furthermore, only idealized point sources or a single, dedicated object [33–37] were investigated. This stands in contrast to the PEPD approach presented in this paper, where the main motivation is to apply aberration retrieval in the context of imaging arbitrary extended objects. Therefore, the Monte Carlo analysis in Ref. [33] is extended and performed for a statistical ensemble that comprises a combination of Gaussian and Poisson noise considering different sets of aberrations as well as different object distributions.

In general, five sets of aberrations are considered, which comprise a combination of N different Zernike modes with a maximum mode number $N=[1, 3, 5, 7, 8]$, excluding piston, tip, and tilt. Each consecutive set includes an additional Zernike mode starting with pure defocus (Z_4) followed by primary astigmatism (Z_5, Z_6), coma (Z_7, Z_8), trefoil (Z_9, Z_{10}), and spherical aberration (Z_{11}). Each set contains 500 randomly generated aberration vectors α . The coefficients α_n ($n=1, 2, \dots, N$) of the individual aberration vectors α are based on uniformly distributed random variables, which are normalized to result in a pre-defined pupil-averaged rms phase error $\alpha_{\text{total}} = \sqrt{\sum_{n=1}^N \alpha_n^2}$.

The set of considered object distributions is extracted from the ImageNet library [38], which is used widely as an image resource in the area of machine learning and object recognition. The library provides an extensive variety of natural object distributions that can be considered as representative examples for the aberration measurement scenario addressed here. We extract a subset of 500 random images of the latest library addition, which contains the newest 5500 images of the overall image library. These images are further processed before they are applied for the Monte Carlo analysis. Initially, each of the eight-bit RGB images is converted to a grayscale format. The resulting images are subsequently cropped to fit a square format and rescaled using a linear interpolation to provide a common resolution of 512×512 pixels.

All calculations consider a combination of idealized (Gaussian) camera readout noise, which is determined by an rms value σ_r , and photon shot-noise, which depends on the

number of photons K_m per channel. A fixed rms readout noise $\sigma_r = 10$ photons per pixel is assumed for all simulations. The number of photons K_m is selected by a pre-defined image SNR. For an extended scene sampled by $P \times P$ pixels, the SNR is defined as the ratio between the average signal and the standard deviation of the signal. It can be expressed for the idealized case of a uniform (white) object distribution by

$$\text{SNR} = \frac{K_m/P^2}{\sqrt{K_m/P^2 + \sigma_r^2}}. \quad (6)$$

The following numerical investigations analyze two different figures of merit for the Monte Carlo performance evaluation. First, the CRLB performance is analyzed, which is commonly used in order to quantify and compare the highest-achievable precision limit. Second, the aberration retrieval SR is investigated as an alternative, practical figure of merit.

B. CRLB Performance

The analysis of Fisher information and the CRLB has been applied previously in the context of PD for optimizing the amount of defocus diversity [33,35,37] or for comparing different diversity modes [34]. It provides the precision limit of the phase retrieval in the presence of image noise in terms of a statistical process. The CRLB with respect to PD aberration measurement has, so far, been investigated only for objects that are known *a priori* [33–35,37]. In contrast, the aberration estimation problem for an unknown object is comparable to a blind deconvolution problem.

The Fisher matrix for a multi-channel, blind deconvolution problem has been derived in the context of orientation estimation for imaged space objects [39]. It can be expressed as

$$[\text{F}(\beta)]_{kl} = \sum_m \sum_{\mathbf{x}} \frac{1}{\tilde{i}(\mathbf{x}) + \sigma_r^2} \frac{\partial \tilde{i}_m(\mathbf{x})}{\partial \beta_k} \frac{\partial \tilde{i}_m(\mathbf{x})}{\partial \beta_l}, \quad (7)$$

considering the PD imaging system described in Section 2. Here, β is the set of unknown system parameters, and σ_r is the rms value of the additive Gaussian noise. The parameters β_k can be divided into two subsets for the general PD wavefront measurement with an unknown object described here. The first subset consists of the previously introduced Zernike aberration coefficients α_n ($n = 1, 2, \dots, N$). The second subset is dedicated to the object distribution described by a set of adequate basis functions. Although the object distribution itself shall not be estimated in the frame of this work, it is nevertheless important to take these parameters into consideration, which can be referred to as *nuisance parameters*. They need to be estimated jointly with the actual parameters of interest (explicitly or implicitly), if *a priori* information on the object is not available [39–41], which we will assume in the following. In this case, we will show that CRLB performance of the aberration estimation is significantly degraded due to the unknown object. One particular set of basis functions to describe the object distribution, which has been used to assess the CRLB for blind deconvolution problems [42], is provided by delta distributions that simply correspond to the discrete sampling locations x_k of the object. However, this basis results in very large Fisher matrices with a total size of $(P^2 + N)^2$ elements. Considering the resolution of

512×512 pixels of the image set used here and seven Zernike aberration modes to be retrieved, a double precision matrix would have a size of 512 GB, which cannot be efficiently handled numerically. In order to reduce the numerical complexity, a transition into the Fourier domain is performed, and a general property of natural objects is exploited. In particular, their power spectral density significantly decreases with higher spatial frequencies, and most of the object information is contained in a low spatial frequency sub-region of the spectrum. Accordingly, it is sufficient to consider only low spatial frequency coefficients Ω_k of the object spectrum to obtain an adequate approximation of the CRLB. The coefficients Ω_k comprise a real part Ω_k^{\Re} and an imaginary part Ω_k^{\Im} , since the Fourier transform $\Omega = \mathcal{F}(o)$ of the object distribution is complex valued. Yet, only half of the Fourier coefficients are considered, because the real valued object distribution o implies that its Fourier transform Ω is Hermitian.

On one hand, the partial derivatives of $\tilde{i}(\mathbf{x})$ with respect to the aberration coefficients α_n for a particular PD channel m are derived in Ref. [33] and given by

$$\frac{\partial \tilde{i}_m(\mathbf{x})}{\partial \alpha_n} = -2K_m o_{\text{norm}}(\mathbf{x}) * (\text{Im} \{ G_m^*(\mathbf{x}; \alpha + \Delta_m) \cdot \mathcal{F} [g_m(\mathbf{u}; \alpha + \Delta_m) Z_n] \}). \quad (8)$$

Note that G_m^* denotes the complex conjugate of the Fourier transform of the pupil function $g_m(\mathbf{u})$ as defined in Eq. (2). On the other hand, the partial derivatives with respect to the real part Ω_k^{\Re} of the object's Fourier coefficients can be obtained using Eq. (1):

$$\begin{aligned} \frac{\partial \tilde{i}_m(\mathbf{x})}{\partial \Omega_k^{\Re}} &= \frac{\partial}{\partial \Omega_k^{\Re}} [o(\mathbf{x}) * h_m(\mathbf{x})] \\ &= \frac{\partial}{\partial \Omega_k^{\Re}} [\mathcal{F}\{\Omega(\mathbf{u}) \cdot H_m(\mathbf{u})\}] \\ &= \frac{\partial}{\partial \Omega_k^{\Re}} \left[\mathcal{F} \left\{ \sum_l (\Omega_l \cdot H_{m,l} \cdot \delta(\mathbf{u} - \mathbf{u}_l)) \right\} \right], \quad (9) \end{aligned}$$

where the Fourier spectrum of $\Omega(\mathbf{u})H_m(\mathbf{u})$ is decomposed into discrete sampling frequencies \mathbf{u}_l using the delta distribution $\delta(\mathbf{u})$. Next, the Hermitian symmetry of $\Omega(\mathbf{u})$ and $H_m(\mathbf{u})$ is exploited to derive the final expression of the derivative according to

$$\begin{aligned} \frac{\partial \tilde{i}_m(\mathbf{x})}{\partial \Omega_k^{\Re}} &= \mathcal{F} \{ (H_{m,k} \cdot \delta(\mathbf{u} - \mathbf{u}_k) + H_{m,k}^* \cdot \delta(\mathbf{u} + \mathbf{u}_k)) \} \\ &= 2 \cdot \Re \{ H_{m,k} \cdot e^{2\pi i(\mathbf{u}_k \cdot \mathbf{x})} \}. \quad (10) \end{aligned}$$

The derivative with respect to the imaginary part Ω_k^{\Im} can be derived in an equivalent manner, which results in

$$\frac{\partial \tilde{i}_m(\mathbf{x})}{\partial \Omega_k^{\Im}} = 2 \cdot \Im \{ H_{m,k} \cdot e^{2\pi i(\mathbf{u}_k \cdot \mathbf{x})} \}. \quad (11)$$

The Fisher matrix can now be calculated using Eq. (7) and considering the derivatives provided in Eqs. (8), (10), and (11). The lower bounds ϵ_k of the mean square error of an unbiased

estimate of the parameters $\beta = \{\alpha, \Omega^{\text{Re}}, \Omega^{\text{Im}}\}$ can be found in the diagonal element of the inverted Fisher matrix according to

$$\epsilon_k^2 = \text{Var}(\beta_k) \geq [F^{-1}(\beta)]_{kk}. \quad (12)$$

The CRLB for the measurement of the entire set of N aberration coefficients $\{\alpha\}$ can then be obtained by the sum of the lower bounds $\sum_{k=1}^N \epsilon_k^2$ that correspond to the CRLBs of the N individual Zernike coefficients α_n . We emphasize again that the CRLB of the aberration estimation is affected by the object spectrum coefficients Ω_k , even if the object itself is not being retrieved. This is due to the inversion of the overall Fisher matrix F in Eq. (12), which, in general, contains non-zero, off-diagonal elements.

Accordingly, the CRLB for the aberration estimation depends on the particular object distribution $o(\mathbf{x})$ as well as the actual aberration coefficients α_k . In order to obtain a general figure of merit of the PEPD aberration measurement scenario, we follow the Monte Carlo type approach presented in Ref. [33]. In particular, the CRLBs of an entire, previously defined set, which contains 500 different aberration vectors α and object distributions o , are averaged, and the final CRLB performance measure is given by

$$\epsilon^2 = \frac{1}{L} \sum_{l=1}^L \left[\sum_{k=1}^N \epsilon_{k,l}^2 \right]. \quad (13)$$

This approach can be considered as a suitable method to evaluate the mean-square error performance of the phase estimation for a particular statistical class of aberrations and objects.

The following calculations consider the PEPD system presented in Section 4 for the symmetrical as well as the asymmetrical PD configuration. The analysis is performed for the previously defined set of object distributions and limited to one of the five aberration sets with $N = 7$ modes. It is shown in the next section that this represents the maximum number of modes that can be reliably estimated using the proposed linear retrieval model. An equal photon count of $K = 1.2 \cdot 10^8$ is assumed for each channel, which corresponds to a SNR of 20 for a uniform object according to Eq. (6). Furthermore, an overall rms aberration error of $\alpha_{\text{total}} = 0.2$ waves is applied. In addition to the engineered double- and triple-helix PSF designs shown in Fig. 1, the CRLB is investigated for a conventional PSF without a phase element.

Initially, the dependency of the CRLB performance measure ϵ^2 on the size of the considered low spatial frequency sub-region of the object is investigated for a single defocus diversity value of $\Delta_4 = 0.7$ waves. In particular, the radius ρ of the circular sub-region is varied with respect to the optical cutoff frequency $\rho_{\text{cut-off}} = 117$ lp/mm. The corresponding plot is shown in Fig. 4(a). It can be seen that the CRLB significantly increases if a non-zero spatial frequency sub-region is taken into consideration. This indicates that the aberration measurement accuracy for an unknown object is deteriorated in comparison to the case of a known object ($\rho = 0$). The CRLB performance of all

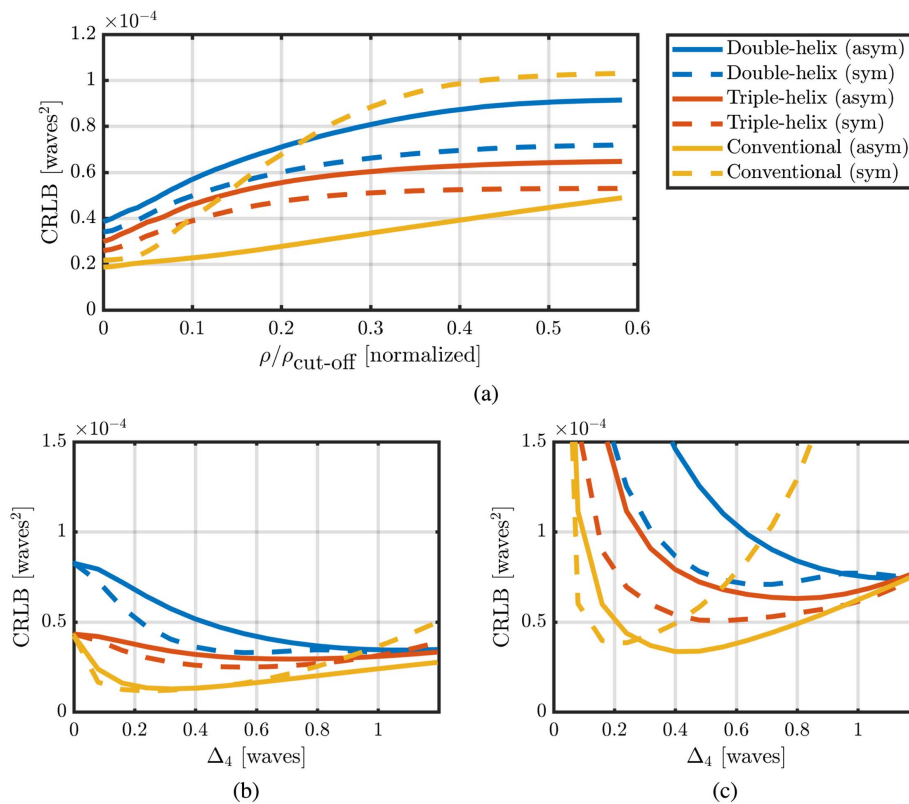


Fig. 4. (a) CRLB dependency on the radius ρ of considered low spatial frequency sub-region of the object for different phase PD aberration retrieval scenarios ($\Delta_4 = 0.7$ waves). (b), (c) CRLB dependency on the selected defocus diversity Δ_4 for the same PD scenarios based on a known and an unknown object distribution, respectively, and considering a low spatial frequency region with $\rho = 0.5 \cdot \rho_{\text{cut-off}}$.

considered PD scenarios converges for radii $\rho > 0.5 \cdot \rho_{\text{cut-off}}$. Accordingly, the subsequent simulations consider only Fourier coefficients Ω_k below this limit to calculate the Fisher matrix, which is considered a suitable approximation of the CRLB performance in order to limit the numerical complexity. Figures 4(b) and 4(c) show the dependency of the corresponding CRLB on the applied defocus diversity Δ_4 in comparison to a known ($\rho = 0$) and an unknown object ($\rho = 0.5 \cdot \rho_{\text{cut-off}}$), respectively. Note that only positive diversity values Δ_4 are plotted here, due to the symmetric CRLB performance, which arises from the uniformly distributed aberration coefficients.

The CRLB analysis for a known object distribution in Fig. 4(b) reveals that the conventional PSF provides a superior performance with respect to the lowest achievable CRLB. The minimum CRLB is approximately a factor of two better than for the triple-helix and a factor of 2.5 better than the double-helix configuration. Note that the symmetrical configuration provides a better minimum CRLB value for all considered pupil functions, which is in agreement with previous results in the literature for the case of a nominal PSF [33]. The results for an unknown object in Fig. 4(c) demonstrate that the CRLB is increased over the entire diversity range in comparison with the case of a known object. Yet, the conventional PSF still provides a superior CRLB performance compared to the helical PSFs.

Both cases demonstrate the existence of an optimum diversity value Δ_4 that provides a minimum CRLB performance. It is pointed out that this optimum is shifted towards larger diversity values for the PEPD systems.

In summary, the conventional motivation for using helical PSFs is based on an improved CRLB for defocus measurements [43–45]. However, the performed simulations indicate that engineered PSFs are inferior when an entire set, i.e., $N = 7$, of aberrations is measured for an extended scene. We note that other authors claim to have found PE PSF designs with a superior performance [46,47] in comparison with the conventional PSF. However, the results of the corresponding analyses are limited. First, the simulations in Refs. [46,47] consider only idealized point sources. On the other hand, the calculation is performed for only a single, non-optimized diversity value Δ_4 . As can be seen from the simulation in Fig. 4, the proper choice of this parameter is crucial when comparing different PD approaches.

C. Aberration Retrieval Performance

The previously performed CRLB investigation aims at determining the precision limit of the measurement in the presence of noise. In a practical adaptive optics or system integration/alignment application scenario, however, it is rather important

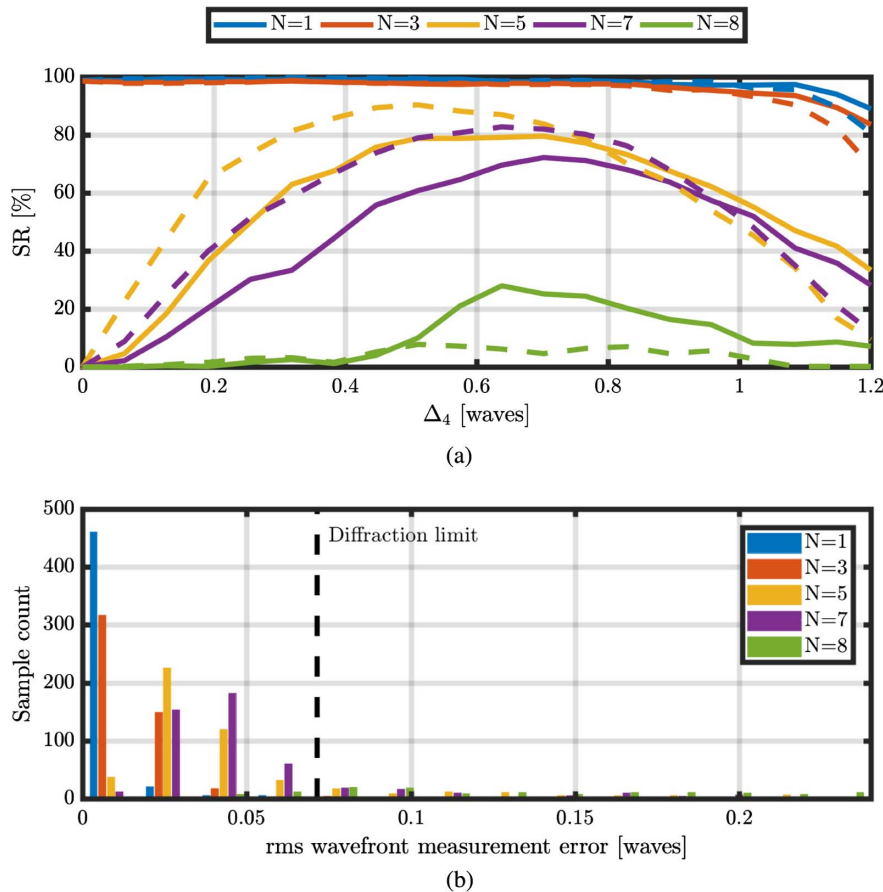


Fig. 5. (a) Dependency of the success rate (SR) on the defocus diversity Δ_4 for the five different aberration sets and comparison between the asymmetrical (solid line) and symmetrical (dashed line) PEPD configurations. (b) Histogram plot illustrating the number of samples of each aberration set that provide a certain rms measurement error for the particular case of a symmetric configuration and $\Delta_4 = 0.7$ waves. An overall wavefront error of $\alpha_{\text{total}} = 0.2$ waves and a photon count of $K_m = 1.2 \cdot 10^8$ are considered.

if the wavefront is correctly measured up to a certain accuracy limit. A suitable limit for classical imaging systems is given by the diffraction limit, which is commonly defined by a residual rms wavefront aberration of $\lambda/(8\sqrt{3})$. Therefore, the aberration retrieval SR is considered for the following performance investigation. It is defined as the relative number of samples of a particular set of aberrations and object distributions with an rms measurement error (deviation between the retrieved and the actual wavefront) below the diffraction limit. Accordingly, it can be interpreted as the probability for a successful aberration retrieval in a practical application scenario, such as co-phasing a segmented optical mirror [19,21].

In order to calculate the SR, the PEPD approach proposed in Section 3 is applied for the previously defined statistical sets of aberration vectors and object distributions. Initially, an equal overall wavefront error of $\alpha_{\text{total}} = 0.2$ waves and photon count $K = 1.2 \cdot 10^8$ compared to the CRLB analysis is considered. The results of the Monte Carlo simulations are shown in Fig. 5(a). The dependency of obtained SR on the defocus diversity Δ_4 is shown for the five different aberration sets and in comparison to the symmetrical and the asymmetrical PEPD configuration. The graphs show that the retrieval of up to three Zernike modes (defocus + astigmatism) provides a SR close to 100% in both scenarios and throughout almost the entire

defocus diversity range under investigation. Note that a similar performance can be obtained using a single channel only. The high SR validates that the cepstrum approach can be used to retrieve the PSF parameters from the acquired images, which confirms that the considered natural objects provide a sufficient amount of small spatial features.

The SR drops for a retrieval of up to seven modes and features distinct optimum diversity values of approximately $\Delta_4 = 0.7$ waves for both scenarios. The appearance of this optimum can be related to the trade-off between the optimum CRLB [Fig. 4(b)] and the condition number assessment [Figs. 3(b) and 3(c)]. The symmetrical configuration provides a superior performance with a SR of up to SR = 84% ($N = 7$), which is in line with the significantly lower condition number compared to the asymmetrical case. The SR deteriorates significantly if spherical aberration is included for the aberration retrieval ($N = 8$). Although, the asymmetrical configuration provides a better performance, the maximum SR is only SR = 30%. The histogram in Fig. 5(b) illustrates how many samples of each set provide a certain rms measurement error for the particular case of a symmetric configuration at $\Delta_4 = 0.65$ waves. The plot indicates that the mean as well as the variance of this error increase with higher maximum mode numbers N . The large spreading for $N = 8$ modes (including spherical aberration) demonstrates

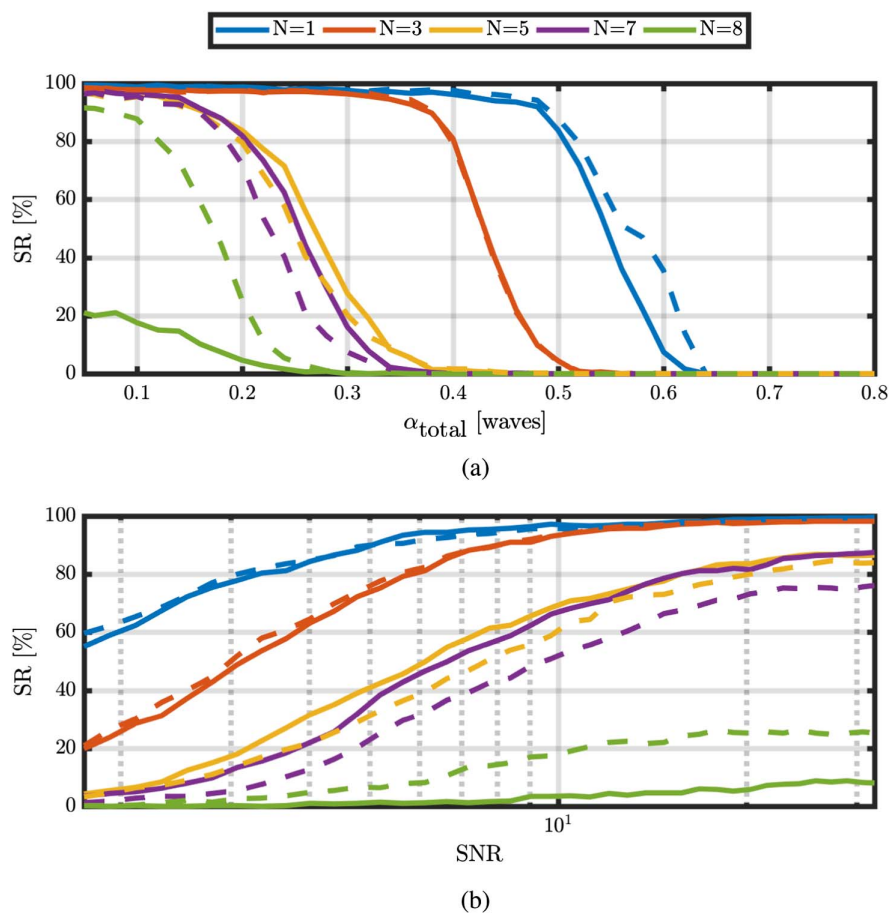


Fig. 6. (a) Dependency of the success rate (SR) on the total wavefront error α_{total} for asymmetrical (solid line) and symmetrical (dashed line) configurations, considering the number of photons per channel $K_m = 1.2 \cdot 10^8$. (b) Dependency of the success rate (SR) on the signal-to-noise ratio for asymmetrical (solid line) and symmetrical (dashed line) configurations, considering a total wavefront error of $\alpha_{\text{total}} = 0.2$ waves. The values are obtained for an optimized defocus diversity of $\Delta_4 = 0.7$ waves.

that the relatively high condition number [Fig. 3(b)] in addition to increased deviation of spherical aberration (Z_{11}) from a linear PSF response (Fig. 2) does not permit a reliable retrieval of that particular mode.

Additional simulations are performed in order to gain further insight into practical limitations of the proposed PEPD approach by analyzing the SR dependency on the total wavefront error α_{total} and the SNR. Figure 6(a) illustrates the dependency of the SR on the total wavefront error α_{total} for asymmetrical and symmetrical configurations. The particular defocus diversity $\Delta_4 = 0.7$ waves is considered, which represents the previously obtained optimum value for $N = 7$. It can be seen that wavefronts that are aberrated by defocus and astigmatism ($N = 3$) can be reliably retrieved up to $\alpha_{\text{total}} = 0.4$ waves. The limit for the retrieval of up to $N = 7$ modes is close to the previously considered total rms wavefront error of $\alpha_{\text{total}} = 0.2$ waves. Figure 6(a) further indicates that wavefronts including spherical aberration (Z_{11}) could be retrieved in an asymmetrical PEPD configuration for small rms errors of $\alpha_{\text{total}} < 0.1$ waves. Finally, the dependency of the SR on the SNR is investigated in Fig. 6(b) for an equal defocus diversity $\Delta_4 = 0.7$ waves and $\alpha_{\text{total}} = 0.2$ waves. To this end, the SNR is scaled by adjusting the number of detected photons K_m per channel according to Eq. (6). Wavefronts that are aberrated by defocus and astigmatism ($N = 3$) can be reliably retrieved with a SR greater than 80% down to a very low SNR ≈ 5 for a symmetrical configuration. The same SR performance necessitates SNR ≈ 20 for $N = 7$. This result demonstrates the robustness of the presented aberration retrieval approach in the presence of considerable image noise. For comparison, the numerical simulations performed for the validation of the deep learning method proposed in Ref. [26] considered only a negligible noise level that corresponds to SNR = 10^5 .

In summary, the performed numerical investigation of the SR shows that the proposed PEPD approach provides an efficient and practical method that can be applied to retrieve wavefronts dominated by low-order Zernike modes up to $N = 7$ (excluding piston, tip, and tilt).

5. EXPERIMENTAL RESULTS

An optical setup characterized by the same parameters as the previously simulated system is implemented experimentally using a commercially available lens (THORLABS achromate AC254-150-A-ML) in combination with a commercially available machine vision CMOS camera (IDS MuEye). The camera provides a resolution of 2456×2054 pixels with a size of $3.45 \mu\text{m}$. The iris aperture stop is placed 55 mm in front of the lens. Note that the nominal system provides a diffraction limited performance over the entire field of view. The same phase element as used in Ref. [30] is placed inside the aperture stop to generate the triple-helix PSF. The element consists of a thin, surface structured borosilicate glass sample and provides low intrinsic aberrations of the transmitted wavefront. A sketch of the optical setup is shown in Fig. 7. A set of low-order, field dependent aberrations is introduced into the experimental optical setup by applying a combination of two different measures. On one hand, the achromatic lens is moved laterally in x direction away from the optical axis defined by the center of

the aperture stop, as indicated in Fig. 7. The image shift, which can be associated with tip and tilt aberrations, is neglected. Only Zernike coefficients associated with defocus, coma, and astigmatism are considered, which constitute the dominating aberration modes that are introduced. On the other hand, the achromatic lens is utilized in a reverse direction, which results in an increased amount of first-order coma and astigmatism. Note that the spherical aberration as well as higher-order modes remain negligible ($\alpha_n < \lambda/50$) due to the high system F-number and small field of view. In summary, the aberrations introduced to the experimental system by a certain lens shift Δx can be understood as a particular sample of the previously investigated aberration set with $N = 5$. Note that the misalignment of an optical system via introducing an element shift or tilt is commonly used to practically evaluate the PD aberration measurement performance [20,48].

The introduced aberrations are initially measured based on imaging a point source object. This makes a quantitative comparison possible between the proposed PEPD method and a conventional aberration retrieval based on a least-square PSF fit. Subsequently, an extended object scene is considered, and the method's capability for retrieving field dependent aberration coefficients for an unknown object is tested. Only the symmetrical PD scenario is considered for both experiments, due to the superior performance compared to the asymmetric configuration, as discussed in Section 4.C.

A. Point Object Approach Verification

A point object is experimentally realized by a combination of a high-power LED source ($\lambda = 540 \text{ nm}$) and a pinhole with a diameter of $20 \mu\text{m}$. This assembly is placed at a nominal distance of 1.8 m in front of the experimental setup, which results in a demagnification factor of 11.9 between the object and the image plane. The pinhole cannot be resolved by the optical setup and therefore provides an adequate point source. A set of 20 images of the point object with different noise realizations is acquired at two image planes, symmetrically located $\pm 2.0 \text{ mm}$ around the nominal focus position, using the triple-helix PSF. This distance from the nominal focus corresponds to a defocus diversity of $\Delta_4 = 0.53$ waves, which is close to the optimum value for $N = 5$ found in the numerical simulations for $N = 5$. The average distributions of the acquired images are illustrated in the top part of Fig. 8 for different amounts of introduced lens shift Δx .

The aberration coefficients for defocus, primary astigmatism, and coma are retrieved based on the proposed linear PEPD approach. The simulated linear transfer matrix \hat{T} and the nominal cepstrum peak position $(\mathbf{x}^c, \mathbf{y}^c)_{m,0}$, obtained in Section 3, are used. The bottom part of Fig. 8 shows the measured aberration coefficients α_n of the relevant Zernike modes ($N = 5$) as well as the total wavefront error α_{total} depending on the introduced lens shift up to 3.5 mm. The small errorbars, which correspond to the statistical rms deviation of the retrieved coefficients for the 20 images, indicate a high relative accuracy of the retrieval.

In order to validate the proposed approach and to evaluate the absolute precision, a comparison with a conventional MLE

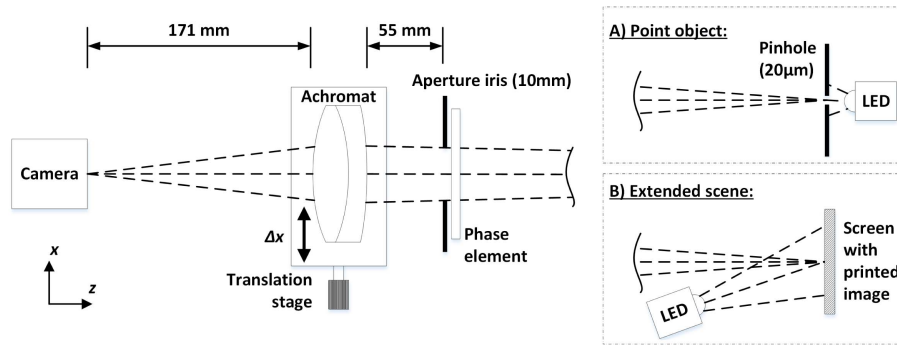


Fig. 7. Sketch of the optical setup applied for testing the PEPD method based on imaging (a) a point object and (b) an extended scene. Note that the distance between the phase element and (a) the pinhole and (b) the extended screen is 1.8 m.

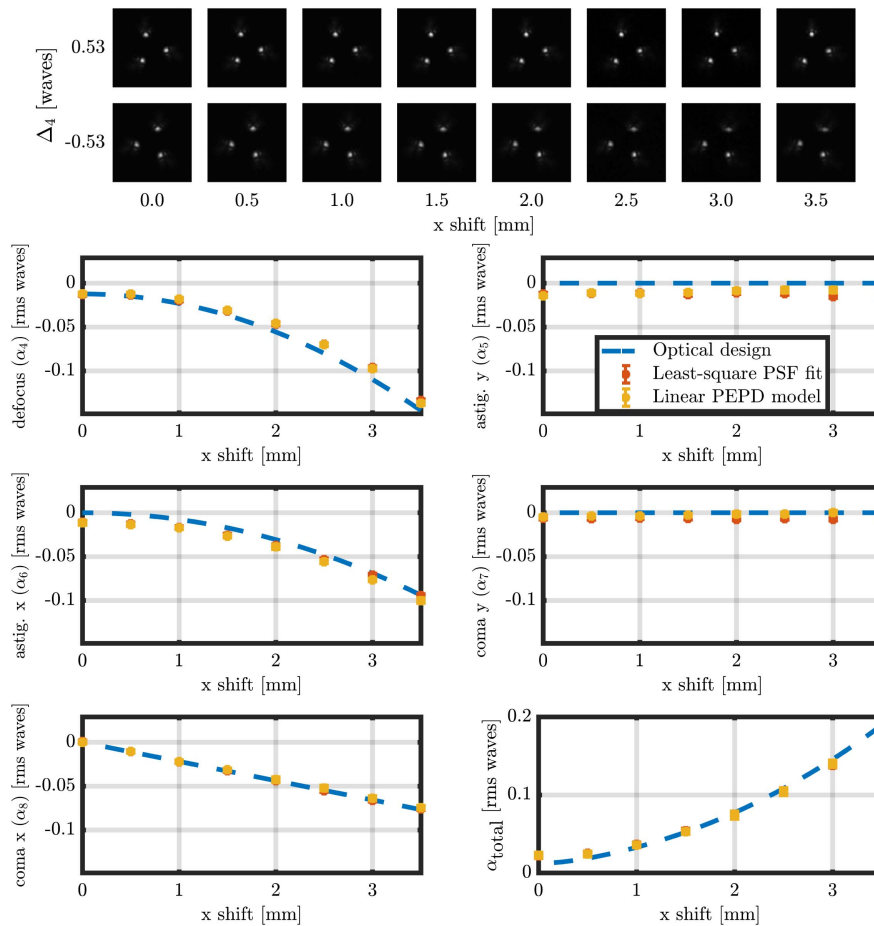


Fig. 8. Top: measured triple-helix PSF distributions for the two considered diversity channels and for different amounts of introduced lens shift Δx . Bottom: comparison of the retrieved Zernike aberration coefficients α_n and the measured total rms wavefront error α_{total} for different amounts of introduced lens shift Δx .

method is performed. In particular, the MLE aberration coefficients are determined by minimizing the mean-square error metric:

$$E = \sum_{m=1}^2 \sum_{\mathbf{x}} \left[h_{m\lambda}(\mathbf{x}) - \hat{h}_{m\lambda}(\mathbf{x}) \right]^2, \quad (14)$$

which is also used for conventional PD [14]. The measured and the estimated PSFs are denoted by $h_m(\mathbf{x})$ and $\hat{h}_m(\mathbf{x})$, respectively. The latter is related to the aberrated, triple-helix pupil

function according to Eq. (4). In addition to the experimental part, the validation of the PEPD method is performed by comparing the measured aberration coefficients to the coefficients extracted from simulating the setup using a standard, optical design software (OpticStudio). As can be seen in the bottom part of Fig. 8, the values of the obtained coefficients using the proposed PEPD method agree well with the reference values obtained by the MLE and the simulations. The maximum absolute deviation between the fit and the linear PEPD is on

the order of $\lambda/100$ and, therefore, demonstrates a successful aberration retrieval.

We emphasize that an accurate knowledge of the basic system parameters is essential for a successful aberration retrieval, which is a well-known practical limitation of PD. In particular, an uncertainty in the nominal focus position leads to an equal estimation error for the defocus aberration coefficient α_4 [49].

Other system parameters that, in general, significantly influence the PD retrieval accuracy include the exit pupil size and location [49]. However, we find that a deviation of 10% between the considered parameters and the true values leads to an additional measurement inaccuracy on the order of only $\lambda/100$ for the system investigated here, if the proposed PEPD method is applied.

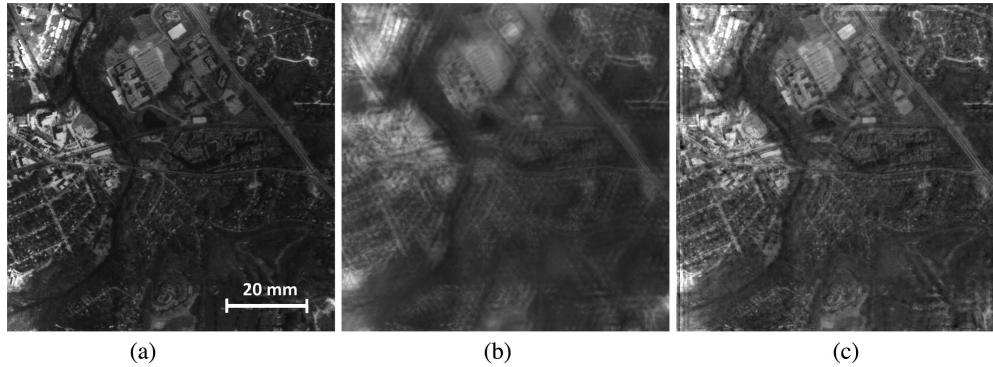


Fig. 9. (a), (b) Raw images of the extended screen captured by the experimental demonstration setup using the nominal PSF and a triple-helix PSF, respectively, for an in-focus diversity channel ($\Delta_4 = 0$ waves). (c) Reconstructed object distribution of the raw image shown in (b) using the Wiener deconvolution approach presented in Ref. [31]. Note that the imaged object scene corresponds to an exemplary, grayscale satellite image printed onto the extended screen with a size indicated by the scale bar in (a).

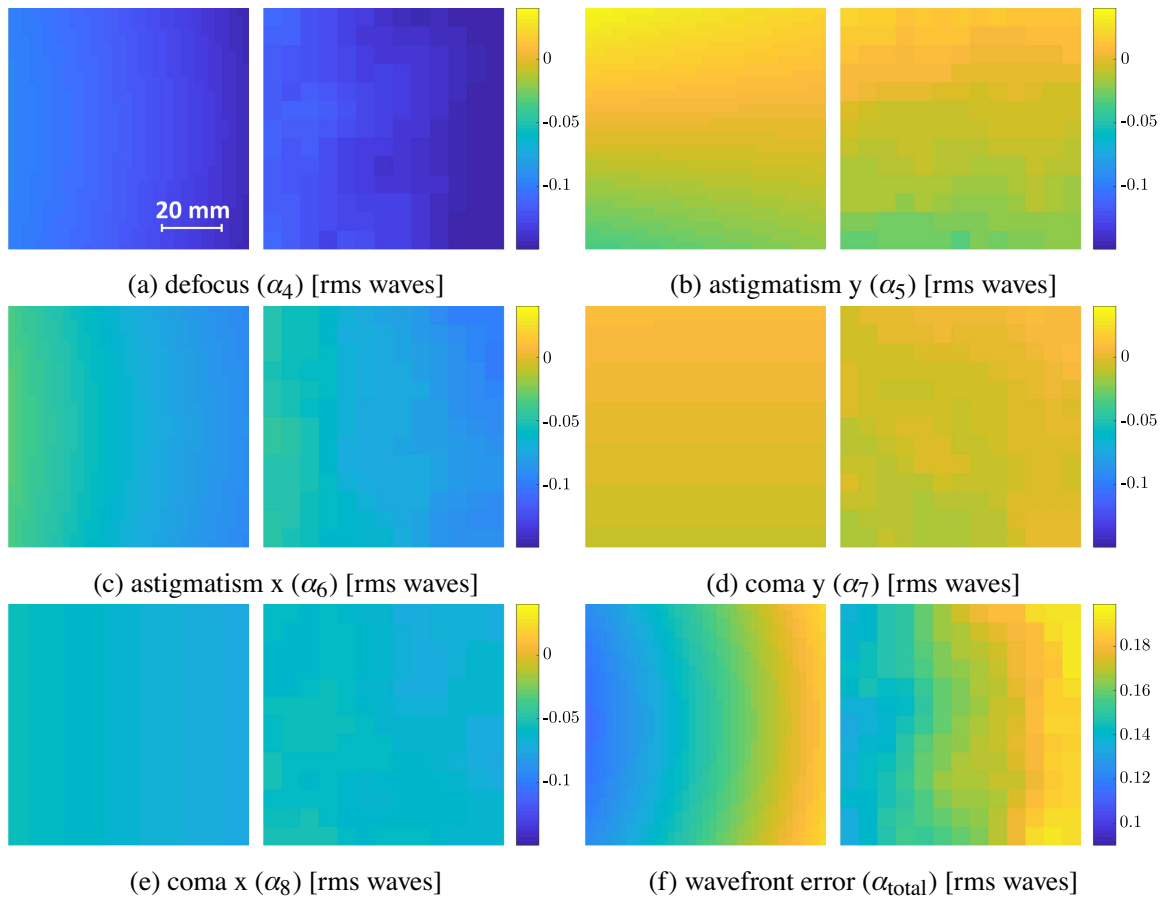


Fig. 10. Comparison of the field dependent aberration coefficients obtained by the proposed linear PEPD model (right columns) and the corresponding values extracted from the optical design (left columns). The aberrations are introduced by shifting the inverted achromatic lens $\Delta x = 3.5$ mm away from the optical axis. The scale bar in (a) indicates the object field extension of the coefficient maps.

B. Extended Scene

The point source assembly used in the previous experiment is replaced by an extended screen that represents an extended object distribution (see Fig. 7). An exemplary, grayscale satellite image is printed onto the extended screen, which is placed at the same object distance of 1.8 m used in the previous experiment. Imaging this particular object distribution may represent a remote sensing application scenario. The printed object scene is illuminated by the previously used high-power LED source. Low-order optical aberrations dominated by defocus, primary astigmatism, and coma are introduced to the optical setup in an equivalent manner compared to the previous experiment by shifting the inverted achromatic lens by 3.5 mm. Figures 9(a) and 9(b) show in-focus, raw camera images of the aberrated scene acquired with a nominal and a triple-helix pupil function, respectively.

In comparison to the previous investigation of a point source, a field dependency of the aberration coefficients α_n needs to be considered for the extended scene. In order to obtain a two-dimensional map of the coefficients based on the proposed power cepstrum analysis, the image segmentation approach used for obtaining depth maps is applied [31]. In particular, the cropped camera image with a size of 2048×2048 pixels is divided into smaller sub-images with a size of 512×512 pixels and a lateral separation of 128 pixels, which leads to an overall aberration map sampling of 13×13 pixels. The local aberration coefficients are calculated for each sub-image based on the proposed, linear PEPD approach using the simulated system parameters \hat{T} and $(\mathbf{x}^c, \mathbf{y}^c)_{m,0}$ and a defocus diversity of $\Delta_4 = 0.53$ waves. The obtained field distributions of the coefficients α_n as well as the total wavefront error α_{total} are directly plotted in Fig. 10. Note that no smoothing was applied. The obtained results can be understood using third-order nodal aberration theory [50]. In contrast to a conventional, rotational symmetric optical system, the introduced lens shift generates distinct nodal points away from the optical axis for field curvature (field dependent defocus), coma, and astigmatism. In particular, the individual image space nodal points for field curvature and coma are located approximately 22 mm and 20 mm away from the image center in negative x direction, respectively. The two nodal points for astigmatism are located approximately 6 mm and 30 mm away from the image center in negative and positive x directions, respectively. Accordingly, the nodal points are located outside the considered sensor width of 7 mm and cannot be observed directly in the plots shown in Fig. 10. The comparison with the theoretical nodal fields extracted from the optical design in Fig. 10, however, shows an agreement of the absolute aberration coefficients and the field dependency. The successful retrieval of field dependent wavefront aberrations (for $N = 5$ up to $\alpha_{\text{total}} \simeq 0.2$ waves) is therefore demonstrated experimentally. The arbitrary, extended scene provides a significantly increased level of complexity in comparison to the simplified objects considered for alternative machine learning methods [13,26]. It is emphasized that the calculation of the entire coefficient distributions can be performed in less than 7s using a conventional laptop due to the fast linear retrieval model.

Depending on the particular application, the actual object distribution $o(\mathbf{x})$ may be of interest in addition to the measured aberration coefficients α_n . The obtained information on the local PSF peak parameters $(\mathbf{x}^c, \mathbf{y}^c)$ can be used to reconstruct the object distribution from the PE image. Figure 9(c) exemplarily shows the reconstructed object distribution for the raw image in Fig. 9(b) using an adapted Wiener deconvolution, as described in Ref. [31]. It can be seen that the effect of the triple-helix PSF, which leads to an overlap of three shifted versions of the object, is removed, and small object features such as individual buildings and roads are retrieved.

6. CONCLUSION

A novel concept that combines conventional PD aberration retrieval with helical PSFs has been presented. It makes a fast estimation of low-order aberration coefficients possible based on imaging an arbitrary, extended (natural) object and solving a linear system of equations. Numerical simulations have been performed, which evaluate the performance of the presented method based on the CRLB and the aberration retrieval SR. To this end, an expression for the CRLB associated with the PD aberration measurement was derived considering an unknown object. Although the CRLB performance of the helical PSFs is inferior in comparison to a conventional PSF, the proposed approach provides a practical tool to estimate the coefficients of up to seven Zernike aberrations with sufficient accuracy (i.e., up to the diffraction limit) without the need for numerically extensive, iterative phase retrieval procedures. The proposed aberration retrieval has been demonstrated experimentally by retrieving the field dependent aberration coefficients for a misaligned optical system based on an unknown, extended scene.

The proposed aberration retrieval method can be understood as an extension of the application scope of helical PSFs. Previous studies targeted the measurement of defocus aberration in order to retrieve depth information. With the method presented here, up to seven aberration modes can be retrieved fast and reliably. The method is considered useful for practical applications including co-phasing of segmented optical mirrors [51], general system alignment, and adaptive optical correction of mechanically or thermally introduced aberrations [52], particularly for cases in which no point source is available. Here, it can be applied to directly characterize and minimize field dependent aberrations (e.g., in a closed loop). Alternatively, it may be used to obtain a robust initial aberration estimate for a conventional iterative PD aberration retrieval approach [14,15]. The results here are obtained with a helical PSF that was originally designed and optimized for depth imaging (defocus measurement over a large range of interest). The performance with respect to the CRLB and the aberration retrieval SR could be further improved by incorporating PSFs that are tailored to the PD problem. As an example, such PSF designs could be optimized with respect to the spot size for only two dedicated defocus diversity positions.

Acknowledgment. We thank Carlas Smith for research advice.

Disclosures. The authors declare no conflicts of interest.

REFERENCES

- W. H. Southwell, "Wave-front analyzer using a maximum likelihood algorithm," *J. Opt. Soc. Am.* **67**, 396–399 (1977).
- J. R. Fienup, "Phase retrieval algorithms: a comparison," *Appl. Opt.* **21**, 2758–2769 (1982).
- J. N. Cederquist, J. R. Fienup, C. C. Wackerman, S. R. Robinson, and D. Kryskowski, "Wave-front phase estimation from Fourier intensity measurements," *J. Opt. Soc. Am. A* **6**, 1020–1026 (1989).
- X. Liu, L. Wang, J. Wang, and H. Meng, "A three-dimensional point spread function for phase retrieval and deconvolution," *Opt. Express* **20**, 15392–15405 (2012).
- B. Ellerbroek and D. Morrison, "Linear methods in phase retrieval," *Proc. SPIE* **0351**, 90–95 (1983).
- C. S. Smith, R. Marinica, A. J. den Dekker, M. Verhaegen, V. Korakiowski, C. U. Keller, and N. Doelman, "Iterative linear focal-plane wavefront correction," *J. Opt. Soc. Am. A* **30**, 2002–2011 (2013).
- A. Polo, A. Haber, S. F. Pereira, M. Verhaegen, and H. P. Urbach, "Linear phase retrieval for real-time adaptive optics," *J. Eur. Opt. Soc.* **8**, 13070 (2013).
- D. Yue, H. Nie, Y. Li, and C. Ying, "Fast correction approach for wavefront sensorless adaptive optics based on a linear phase diversity technique," *Appl. Opt.* **57**, 1650–1656 (2018).
- H. Guo, N. Korablinova, Q. Ren, and J. Bille, "Wavefront reconstruction with artificial neural networks," *Opt. Express* **14**, 6456–6462 (2006).
- S. W. Paine and J. R. Fienup, "Machine learning for improved image-based wavefront sensing," *Opt. Lett.* **43**, 1235–1238 (2018).
- G. Ju, X. Qi, H. Ma, and C. Yan, "Feature-based phase retrieval wavefront sensing approach using machine learning," *Opt. Express* **26**, 31767–31783 (2018).
- S. Lohani and R. T. Glasser, "Turbulence correction with artificial neural networks," *Opt. Lett.* **43**, 2611–2614 (2018).
- Y. Nishizaki, M. Valdivia, R. Horisaki, K. Kitaguchi, M. Saito, J. Tanida, and E. Vera, "Deep learning wavefront sensing," *Opt. Express* **27**, 240–251 (2019).
- R. A. Gonsalves, "Phase retrieval and diversity in adaptive optics," *Opt. Eng.* **21**, 215829 (1982).
- L. M. Mugnier, A. Blanc, and J. Idier, "Phase diversity: a technique for wave-front sensing and for diffraction-limited imaging," *Adv. Imag. Elect. Phys.* **141**, pp. 1–76 (2006).
- R. G. Paxman, T. J. Schulz, and J. R. Fienup, "Joint estimation of object and aberrations by using phase diversity," *J. Opt. Soc. Am. A* **9**, 1072–1085 (1992).
- A. Blanc, L. M. Mugnier, and J. Idier, "Marginal estimation of aberrations and image restoration by use of phase diversity," *J. Opt. Soc. Am. A* **20**, 1035–1045 (2003).
- M. W. Smith, "Use of adaptive optics to implement non quadratic phase diversity imaging," *Proc. SPIE* **5524**, 66–77 (2004).
- R. L. Kendrick, D. S. Acton, and A. L. Duncan, "Phase-diversity wavefront sensor for imaging systems," *Appl. Opt.* **33**, 6533–6546 (1994).
- N. Miyamura, "Generalized phase diversity method for self-compensation of wavefront aberration using spatial light modulator," *Opt. Eng.* **48**, 128201 (2009).
- M. R. Bolcar and J. R. Fienup, "Sub-aperture piston phase diversity for segmented and multi-aperture systems," *Appl. Opt.* **48**, A5–A12 (2009).
- J.-F. Sauvage, L. Mugnier, B. Paul, and R. Villecroze, "Coronagraphic phase diversity: a simple focal plane sensor for high-contrast imaging," *Opt. Lett.* **37**, 4808–4810 (2012).
- H. Yang, O. Soloviev, and M. Verhaegen, "Model-based wavefront sensorless adaptive optics system for large aberrations and extended objects," *Opt. Express* **23**, 24587–24601 (2015).
- D. Wilding, P. Pozzi, O. Soloviev, G. Vdovin, and M. Verhaegen, "Pupil mask diversity for image correction in microscopy," *Opt. Express* **26**, 14832–14841 (2018).
- I. Moccœur, L. M. Mugnier, and F. Cassaing, "Analytical solution to the phase-diversity problem for real-time wavefront sensing," *Opt. Lett.* **34**, 3487–3489 (2009).
- Q. Xin, G. Ju, C. Zhang, and S. Xu, "Object-independent image-based wavefront sensing approach using phase diversity images and deep learning," *Opt. Express* **27**, 26102–26119 (2019).
- C. Roider, R. Piestun, and A. Jesacher, "3D image scanning microscopy with engineered excitation and detection," *Optica* **4**, 1373–1381 (2017).
- C. Smith, M. Huisman, M. Siemons, D. Grünwald, and S. Stallinga, "Simultaneous measurement of emission color and 3D position of single molecules," *Opt. Express* **24**, 4996–5013 (2016).
- S. R. P. Pavani, M. A. Thompson, J. S. Biteen, S. J. Lord, N. Liu, R. J. Twieg, R. Piestun, and W. E. Moerner, "Three-dimensional, single-molecule fluorescence imaging beyond the diffraction limit by using a double-helix point spread function," *Proc. Natl. Acad. Sci. USA* **106**, 2995–2999 (2009).
- R. Berlich and S. Stallinga, "High-order-helix point spread functions for monocular three-dimensional imaging with superior aberration robustness," *Opt. Express* **26**, 4873–4891 (2018).
- R. Berlich, A. Bräuer, and S. Stallinga, "Single shot three-dimensional imaging using an engineered point spread function," *Opt. Express* **24**, 5946–5960 (2016).
- Z. Wang, Y. Cai, Y. Liang, D. Dan, B. Yao, and M. Lei, "Aberration correction method based on double-helix point spread function," *J. Biomed. Opt.* **24**, 031005 (2019).
- D. J. Lee, M. C. Roggemann, and B. M. Welsh, "Cramér–Rao analysis of phase-diverse wave-front sensing," *J. Opt. Soc. Am. A* **16**, 1005–1015 (1999).
- J. J. Dolne and H. B. Schall, "Cramer–Rao bound and phase-diversity blind deconvolution performance versus diversity polynomials," *Appl. Opt.* **44**, 6220–6227 (2005).
- S. Prasad, "Fisher-information-based analysis of a phase-diversity-speckle imaging system," *J. Opt. Soc. Am. A* **21**, 2073–2088 (2004).
- J. J. Dolne, "Evaluation of the phase diversity algorithm for noise statistics error and diversity function combination," *Proc. SPIE* **6307**, 630708 (2006).
- B. H. Dean and C. W. Bowers, "Diversity selection for phase-diverse phase retrieval," *J. Opt. Soc. Am. A* **20**, 1490–1504 (2003).
- O. Russakovsky, J. Deng, H. Su, J. Krause, S. Satheesh, S. Ma, Z. Huang, A. Karpathy, A. Khosla, M. Bernstein, A. C. Berg, and L. Fei-Fei, "ImageNet large scale visual recognition challenge," *Int. J. Comput. Vision* **115**, 211–252 (2015).
- D. R. Gerwe and P. S. Idell, "Cramér–Rao analysis of orientation estimation: viewing geometry influences on the information conveyed by target features," *J. Opt. Soc. Am. A* **20**, 797–816 (2003).
- S. M. Kay, *Fundamentals of Statistical Signal Processing: Estimation Theory* (1993), Vol. I.
- D. R. Gerwe, J. L. Hill, and P. S. Idell, "Cramér–Rao analysis of orientation estimation: influence of target model uncertainties," *J. Opt. Soc. Am. A* **20**, 817–826 (2003).
- C. L. Matson, K. Borelli, S. Jefferies, C. C. Beckner, E. K. Hege, and L. H. Michael, "Fast and optimal multiframe blind deconvolution algorithm for high-resolution ground-based imaging of space objects," *Appl. Opt.* **48**, A75–A90 (2009).
- M. Badirostami, M. D. Lew, M. A. Thompson, and W. E. Moerner, "Three-dimensional localization precision of the double-helix point spread function versus astigmatism and biplane," *Appl. Phys. Lett.* **97**, 161103 (2010).
- S. R. P. Pavani, A. Greengard, and R. Piestun, "Three-dimensional localization with nanometer accuracy using a detector-limited double-helix point spread function system," *Appl. Phys. Lett.* **95**, 021103 (2009).
- G. Grover, S. R. P. Pavani, and R. Piestun, "Performance limits on three-dimensional particle localization in photon-limited microscopy," *Opt. Lett.* **35**, 3306–3308 (2010).
- M. K. Sharma, C. Gaur, P. Senthikumar, and K. Khare, "Phase imaging using spiral-phase diversity," *Appl. Opt.* **54**, 3979–3985 (2015).
- S. Echeverri-Chacón, R. Restrepo, C. Cuartas-Vélez, and N. Uribe-Patarroyo, "Vortex-enhanced coherent-illumination phase diversity

- for phase retrieval in coherent imaging systems,” *Opt. Lett.* **41**, 1817–1820 (2016).
48. J. J. Dolne, R. J. Tansey, K. A. Black, J. H. Deville, P. R. Cunningham, K. C. Widen, and P. S. Idell, “Practical issues in wave-front sensing by use of phase diversity,” *Appl. Opt.* **42**, 5284–5289 (2003).
49. A. Blanc, T. Fusco, M. Hartung, L. M. Mugnier, and G. Rousset, “Calibration of NAOS and CONICA static aberrations. Application of the phase diversity technique,” *Astron. Astrophys.* **399**, 373–383 (2003).
50. K. Thompson, “Description of the third-order optical aberrations of near-circular pupil optical systems without symmetry,” *J. Opt. Soc. Am. A* **22**, 1389–1401 (2005).
51. L. D. Feinberg, B. H. Dean, D. L. Aronstein, C. W. Bowers, W. Hayden, R. G. Lyon, R. Shiri, J. S. Smith, D. S. Acton, L. Carey, A. Contos, E. Sabatke, J. Schwenker, D. Shields, T. Towell, F. Shi, and L. Meza, “TRL-6 for JWST wavefront sensing and control,” *Proc. SPIE* **6687**, 668708 (2007).
52. N. Devaney, C. Reinlein, N. Lange, M. Goy, A. Goncharov, and P. Hallibert, “HYPATIA and STOIC: an active optics system for a large space telescope,” *Proc. SPIE* **9904**, 990469 (2016).